crystals

MDPI

Article

Ferroelectric Domain Intrinsic Radiation Resistance of Lithium Niobate Ferroelectric Single−Crystal Film

Jiahe Li [1], Jinlong He [2], Liya Niu [3], Hao Lu [1], Xiaojun Qiao [1,4], Bo Zhong [1], Mingzhu Xun [5], Xiujian Chou [1] and Wenping Geng [1,*]

[1] Science and Technology on Electronic Test and Measurement Laboratory, North University of China, Taiyuan 030051, China; s202206068@st.nuc.edu.cn (J.L.); xiaojunqiao@nuc.edu.cn (X.Q.)
[2] Faraday Technology Corporation SZ, Suzhou 215123, China; s1906190@st.nuc.edu.cn
[3] Jiangsu Institute of Advanced Semiconductors Ltd., Suzhou 215123, China; s2006132@st.nuc.edu.cn
[4] Guangdong Institute of Semiconductor Micro−Nano Manufacturing Technology, Foshan 528000, China
[5] Xinjiang Technical Institute of Physics and Chemistry, Chinese Academy of Sciences, Urumchi 830011, China; xunmz@ms.xjb.ac.cn
* Correspondence: wenpinggeng@nuc.edu.cn

Abstract: The study of the properties of ferroelectric materials against irradiation has a long history. However, anti−irradiation research on the ferroelectric domain has not been carried out. In this paper, the irradiation of switched domain structure is innovatively proposed. The switched domain of 700 nm lithium niobate ($LiNbO_3$, LN) thin film remains stable after gamma irradiation from 1 krad to 10 Mrad, which was prepared by piezoresponse force microscopy (PFM). In addition, the changing law of domain wall resistivity is explored through different sample voltages, and it is verified that the irradiated domain wall conductivity is still larger than the domain. This domain wall current (DWC) property can be applied to storage, logic, sensing, and other devices. Based on these, a ferroelectric domain irradiation resistance model is established, which explains the reason at an atomic level. The results open a possibility for exploiting ferroelectric materials as the foundation in the application of space and nuclear fields.

Keywords: ferroelectric; gamma irradiation; domain wall current; $LiNbO_3$

Citation: Li, J.; He, J.; Niu, L.; Lu, H.; Qiao, X.; Zhong, B.; Xun, M.; Chou, X.; Geng, W. Ferroelectric Domain Intrinsic Radiation Resistance of Lithium Niobate Ferroelectric Single−Crystal Film. *Crystals* **2024**, *14*, 537. https://doi.org/10.3390/cryst14060537

Academic Editor: Serguei Petrovich Palto

Received: 27 April 2024
Revised: 21 May 2024
Accepted: 5 June 2024
Published: 7 June 2024

1. Introduction

MEMS devices are widely utilized in various fields such as space, nuclear imaging, and radiotherapy, owing to their ultrafine integration process, miniaturization, low cost, high reliability, and batch manufacturing capabilities [1–3]. Traditional silicon−based MEMS devices typically incorporate SiO_2 oxide insulating layers, crucial for device performance, but susceptible to radiation−induced effects [4–6]. High−energy particles make electrons leave their original positions under irradiation. New electron−hole pairs are formed which increases the leakage current [7]. At the same time, high−energy particles may also break the Si−O bond and form the Si−Si bond, resulting in irreversible damage to the oxide layer [8]. Irradiation−resistant reinforcement is becoming increasingly important to reduce the effects of ionizing irradiation on conventional MEMS devices, but the package of anti−irradiation will enlarge the size of the device seriously which hinders its integration [9–11]. Therefore, it is urgent to explore novel functional materials that possess the character of anti−irradiation and compatibly integrate. Ferroelectric materials have been proven to have strong irradiation resistance in the last century [12,13]. A PZT thin film received gamma irradiation of 5 Mrad by J. F. Scott et al. A surprising result was that the polarization had almost no decline and the hysteresis curves became more symmetric [14]. In recent years, single crystal $LiNbO_3$ began to attract people's attention which can be attributed to its unique characteristics. One of them is that the surface potential can be controlled by the domain. Lei Tong et al. designed a nonlinear

transistor prepared by combining 2D material and periodically poled lithium niobate (PPLN). Then, they used this transistor in neuromorphic hardware that integrates memory and logic [15]. Domain wall current (DWC) is another characteristic of single−crystal $LiNbO_3$. It can effectively modulate the bulk conductivity and be creatable, erasable, and repeatable. Based on these great characteristics, the DWC transistor was established by Xiaojie Chai et al., which was a nano−island structure created by X−cut LN. It has a high on–off ratio, high working efficiency, and ultrafast response speed [16]. With the development of nano−scale single−crystal film preparation technology, the LN domain engineering field is also developing rapidly [17–19]. Therefore, memory devices and logic devices based on domains have emerged. A single−crystal LN has only a 180° domain wall, which makes it a natural memory device. In addition, the electrical conductivity of the domain wall is significantly higher than the domain [20–22]. This characteristic is also considered to have great potential in the field of integrated circuits [21]. Liya Niu et al. developed a kind of diode−like cell based on the properties of conducting domain wall diodes. It has an ultra−high output−holding performance and assembles an "OR" logic gate through an array of cells [23]. Jinlong He et al. developed a domain wall temperature sensor based on the property of negative temperature coefficient of conducting domain walls. It has a wide temperature range and high sensitivity with an on−off ratio of up to 10^3 [24]. Single−crystal LN not only has excellent FE properties but is also indispensable in the electro−optic and nonlinear−optic fields [25–27]. In conclusion, the domain of single−crystal LN has a broad application field [28]. However, no research has been carried out on the anti−irradiation of the ferroelectric domain which can develop domain engineering devices.

There is electromagnetic radiation and ionizing radiation in space. Electromagnetic radiation consists of natural radiation (thermal radiation from the Earth, solar thermal radiation, cosmic rays, etc.) and artificial radiation (radar, communication base stations and electromagnetic applications). Ionizing radiation consists of high−speed charged particles (α−particles, β−particles, and protons) and uncharged particles (neutrons, X−ray, and γ−ray). Gamma rays are often considered the standard source of radiation for studying and resolving the effects of irradiation damage in microelectronic devices [29]. Gamma rays are highly penetrative due to their short wavelength, which is on the order of nanometers. When the gamma ray energy is between a few hundred keV and a few MeV, gamma rays in this energy range can penetrate deeply into microelectronic devices and induce the generation of electron−hole pairs, leading to charge accumulation damage. When the energy of gamma rays exceeds 1 MeV, their penetrating ability is further increased, which not only generates secondary electrons in semiconductor materials, but also may cause atomic displacements, leading to severe lattice damage [30].As the core of ferroelectric microelectronic devices, the study of the irradiation resistance of ferroelectric domains and their conducting domain walls can help the wide application of ferroelectric microelectronic devices in the fields of deep−space exploration and nuclear engineering.

In this paper, we mainly focused on LN switched domain structure before and after irradiation. The same switched domain of Z−cut LN thin film was prepared by PFM in five samples. Then, they were irradiated by gamma from 1 krad to 10 Mrad, respectively. The results show that the switched domain structure and DWC have strong irradiation resistance. An atomic irradiation model was established to explain ferroelectric domain irradiation resistance. Our research provides guidelines for the fabrication of LN domain engineering that can cater to applications in harsh environments. It provides a novel pathway for the future application of LN in space and nuclear fields.

2. Materials and Methods

In this work, all of the samples were 700 nm Z−cut LN, which were fabricated by the smart−cut method. Block−like ferroelectric materials are difficult to realize large−scale integrated applications due to their high thickness and large coercive field. Ion implantation−assisted stripping technology has received a lot of attention to obtain ferroelectric single−crystal thin

film materials with micrometer/nanometer thicknesses. The schematic flow of ferroelectric single crystal thin film preparation is outlined in Figure 1. The sacrificial damaged layer of single crystal LN bulk was formed by high energy and high doses of He^+ injection. The depth of ion injection was precisely controlled by adjusting the He^+ injection energy and angle of incidence, enabling the production of thin film materials with controllable thicknesses [31]. The LN bulk with 50 nm sputtering Pt layer bonded to 500 μm LN substrate which possesses 2 μm SiO_2 layer directly. Following annealing, LN thin film was exfoliated at the sacrificial damaged layer. The LN thin film−Pt−SiO_2−LN substrate multi−layer heterostructure was obtained as shown in Figure 1e. Then, the surface roughness was controlled within optical grade by chemical mechanical polishing (CMP) technology. The congruent lithium niobate used in this work was supplied by NANOLN (Jinan, China).

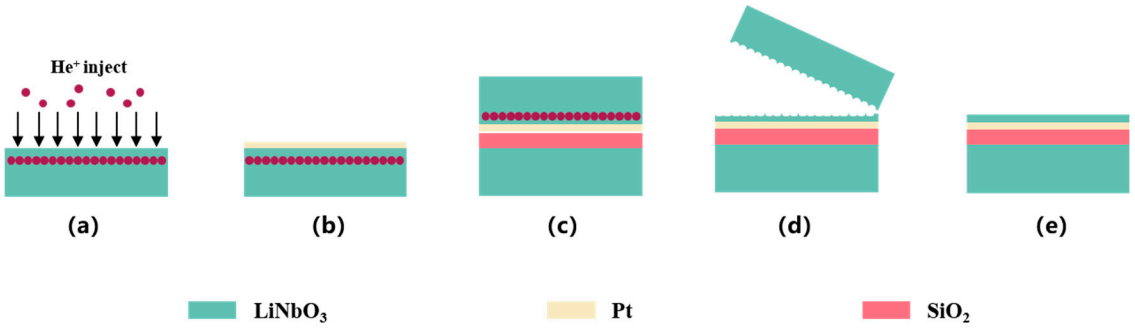

Figure 1. Schematic flow diagram of ferroelectric single crystal thin film preparation process: (**a**) He^+ ion implantation; (**b**) magnetron sputtering 50nmPt; (**c**) direct bonding of LN bulk to substrate; (**d**) annealing, stripping at sacrificial layer; and (**e**) optical grade LN obtained after CMP.

For the characterization of domain structure and domain wall current, atomic force microscopy (MFP−3D Origin Plus, Asylum Research, Santa Barbara, CA, USA) was used in this work. It can be equipped with different modules, including a PFM mode, a litho mode conducting atomic force microscopy (c−AFM) mode, etc. And the probe is a conductive probe that possesses Pt/Ir coating (SCM−PIT−75, Nanoworld, Swiss). The tip radius is ~25 nm, the elastic coefficient is ~2.8 N/m and the resonance frequency is ~75 kHz.

In this study, the switched domains were irradiated using a ^{60}Co gamma radiation source at the Xinjiang Institute of Physics and Chemistry Technology, Chinese Academy of Sciences. In the process of radiation, ^{60}Co will decay, firstly undergoing a β−decay into ^{60}Ni, which is still unstable, and then radiating two γ−photons into the stable state of ^{60}Ni. The energies of the two photons released from the final gamma−ray are 1.17 MeV and 1.33 MeV [32].

3. Results

The spontaneous polarization of ferroelectric materials can be due to the existence of electric dipole moments. The crystal lattice of $LiNbO_3$, a ferroelectric material, exhibits a trigonal structure, as depicted in Figure 2a. Within the $LiNbO_3$ unit cell, Li^+ ions are positioned between two oxygen planes, albeit not at the center, and the same applies to Nb^{5+} ions. When the polarization direction is oriented upwards, Li^+ ions are situated below the midpoint of the two oxygen planes, while Nb^{5+} ions are located above this midpoint [33]. By applying a voltage exceeding the coercive field, the polarization direction can be altered. At this moment, Li^+ ions traverse the underlying oxygen plane to assume a new position above the midpoint of the two oxygen planes, while Nb^{5+} ions move below this midpoint. Therefore, the essence of $LiNbO_3$ domain switching is the movement of Li^+ and Nb^{5+}.

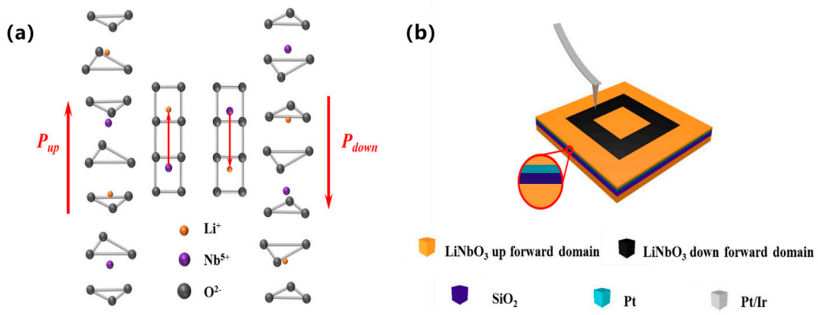

Figure 2. (**a**) Schematic of $LiNbO_3$ ferroelectric crystal lattice; (**b**) schematic diagram of domain switching.

In summary, the process of polarization reversal can be delineated into four distinct stages: nucleation of a new domain, longitudinal growth of the reversed domain, transverse expansion, and domain merging. For 700 nm Z−cut lithium niobate, a new domain occurs along the direction of the applied electric field when an electric field opposite the direction of spontaneous polarization and larger than the coercive field is applied between the upper and lower electrodes. Once polarization is sustained, the newly nucleated domain overcomes energy barriers, facilitating further expansion and eventual merging into regions oriented in the opposite direction to the initial domain. This merging process gives rise to a conducting domain wall between the newly formed domain and the initial one. Figure 2b shows up forward domain switched to the down forward domain by tip voltage.

In the litho mode, preset voltages and patterns facilitate precise switching of the domain. In Figure 3, the custom pattern domain is switched in a 10 μm × 10 μm square by a voltage of ±80 V. The topography, amplitude, and phase image of this area are obtained through a dual−frequency tracking mode (DART SS). All PFM images are composed of 256 × 256 points for quantitative analysis. Figure 3a illustrates the morphology of a single−crystal lithium niobate film after polarization reversal, with a sample rms roughness of 263.03 pm and surface undulations of ~10 nm. Figure 3c displays the polarized domain phase. By employing a customized nested square pattern and a specific voltage, a square switched domain is obtained. The orange and green lines in Figure 3c correspond to Figure 3e, and both lines represent a different phase, which differs by approximately 180°, demonstrating the uniaxial polarization properties of single−crystal lithium niobate films.

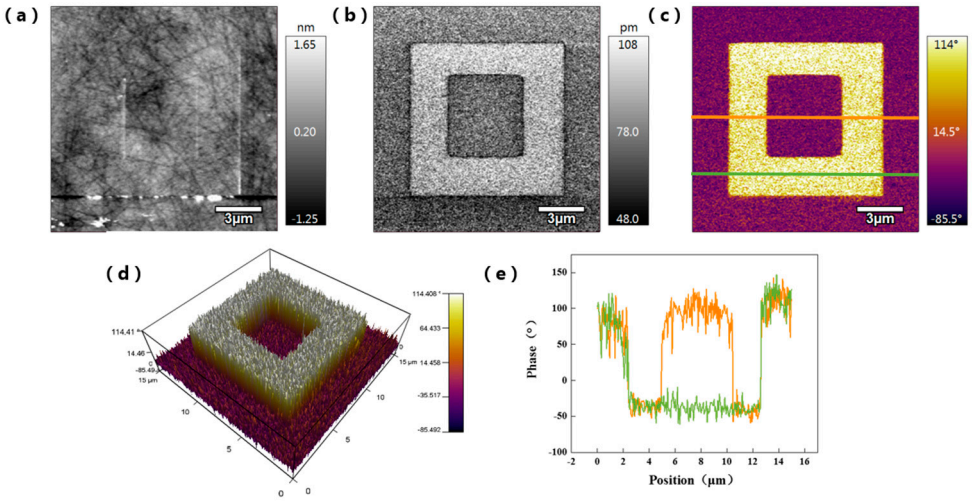

Figure 3. (**a**) Lithium niobate switched domain surface morphology; (**b**) amplitude retrace diagram of lithium niobate switched domain; (**c**) phase diagram of lithium niobate switched domain; (**d**) 3D plot of lithium niobate switched domain phase; (**e**) orange and green cutoffs in (**c**) correspond to phase curve.

To investigate the effects of gamma irradiation at different doses on a switched domain, five identical switched domains were prepared within five bonded thin film samples of LN. Subsequently, they were exposed to gamma irradiation at a rate of 200 rad/s, with total doses ranging from 10 krad to 10 Mrad. Figure 4 shows the switched domain before and after irradiation by various doses of gamma. Remarkably, the domain remained stable even after gamma irradiation, with the opposite direction domain retaining a 180° phase gap. While the gamma irradiation from 1 krad to 100 krad, there was no observable change in the switched domain. Only minor alterations were observed with increasing gamma irradiation from 1 Mrad to 10 Mrad, yet the nested square structure fundamentally remained intact. It was apparent that the domain of $LiNbO_3$ has great irradiation resistance.

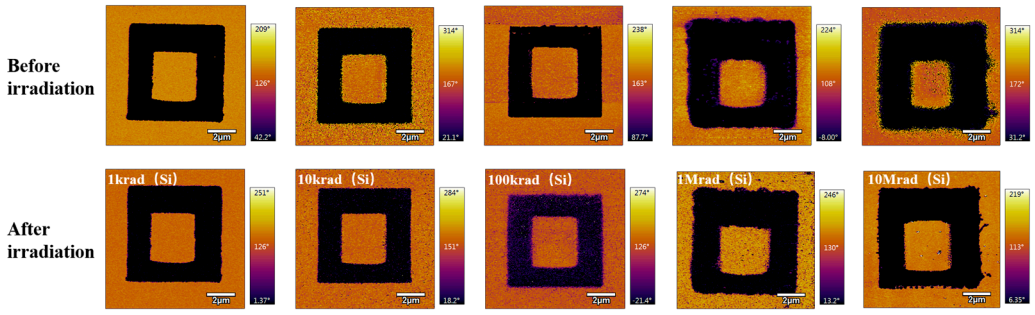

Figure 4. Switched domain before and after 1 krad–10 Mrad gamma irradiation.

All PFM images are composed of 256 × 256 points for quantitative analysis. In this work, the value in the middle of the colour scale of the phase diagram is used as the basis for domain switching or not, and the change in the percentage of switched domains before and after different irradiation doses is derived by counting the percentage of switched domains in 256 × 256 points. A table of changes in the switched domain before and after gamma irradiation from 1 krad to 10 Mrad was obtained in the above manner (Table 1). A comparison of the percentage of switched domains from 1 krad to 1 Mrad of total gamma irradiation dose showed that the change in switched domains before and after irradiation was within 5%. When the total irradiation dose reaches 10 Mrad, the percentage of switched domains fluctuates more before and after irradiation, but the nested square structure remains unchanged.

Table 1. Changes in the percentage of the switched domain before and after different irradiation doses.

Irradiation Dose	Pre−Irradiation	Post−Irradiation	Change in Percentage
1 krad	35.89%	38.71%	2.82%
10 krad	35.20%	35.42%	0.22%
100 krad	31.68%	32.00%	0.32%
1 Mrad	50.08%	48.70%	1.38%
10 Mrad	53.20%	42.84%	10.36%

The domain wall possesses higher electrical conductivity than the domain, but the domain wall is not all conductive. When two polarized regions contact in a head−to−head or tail−to−tail direction to form a domain wall, the injected charge migrates and accumulates at the domain wall, and the domain wall conductivity becomes high. When the polarization directions of both sides of the domain wall are fully parallel, positive and negative charges within the crystal cancel each other out, resulting in nearly insulating properties for the domain wall. In the ORCA mode of the c−AFM, as depicted in Figure 5a, the domain wall current remains consistently weak as the sample voltage increases from −1 V to −4 V, showing no significant enhancement with the increment of the test voltage. As the sampling voltage increases from −5 V to −9 V, the domain wall current increases

significantly in a linear trend. When the sampling voltage is increased from −9 V to −10 V, there is no significant change in the domain wall current. Figure 5b illustrates that the domain wall current does not increase in a linear trend without limit as the sample voltage increases. Since too large negative voltage applied can affect the state of the domain wall current or even lead to sample depolarization, a suitable sample voltage must be chosen to test the domain current. Therefore, a sample voltage of −7 V was chosen for subsequent comparative experiments investigating domain current changes before and after irradiation.

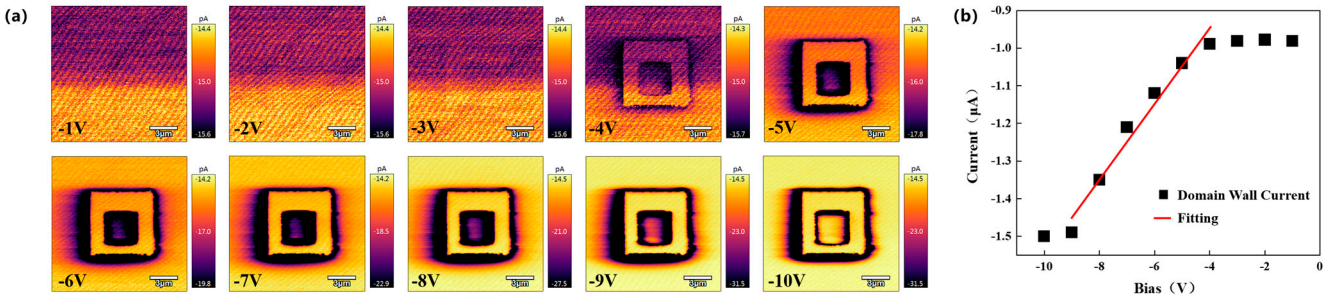

Figure 5. (**a**) Domain wall current with different sample voltage; (**b**) current graph of 10 μm × 10 μm region with different sample voltage.

In ferroelectric materials, domain walls can be erased or built up by external electric fields. Therefore, this property has attracted the attention of scholars. In this work, after gamma irradiation, DWC is shown in Figure 6. Figure 6a illustrates the c−AFM data plot after gamma irradiation ranging from 0 rad to 10 Mrad at a sample voltage of −7 V, accurately depicting the domain wall structure corresponding to the switched domain shown in Figure 4. After gamma irradiation, there still exists higher conductivity at the domain wall. Figure 6b illustrates the domain wall currents in a 10 μm × 10 μm region at a sample voltage of −7 V under different doses of gamma irradiation. From 0 rad to 10 Mrad, the domain wall currents are −1.27 μA, −1.07 μA, −1.20 μA, −1.59 μA, −1.63 μA and −1.21 μA, respectively. Notably, the fitting line tends to be constant. From Figure 6b, it can be seen that the domain wall currents are still not significantly weakened after 10 Mrad gamma irradiation, which proves the anti−ionizing irradiation performance of the switched domains of single−crystal lithium niobate films. These results suggest that DWC, like domain, exhibits high resistance to gamma irradiation.

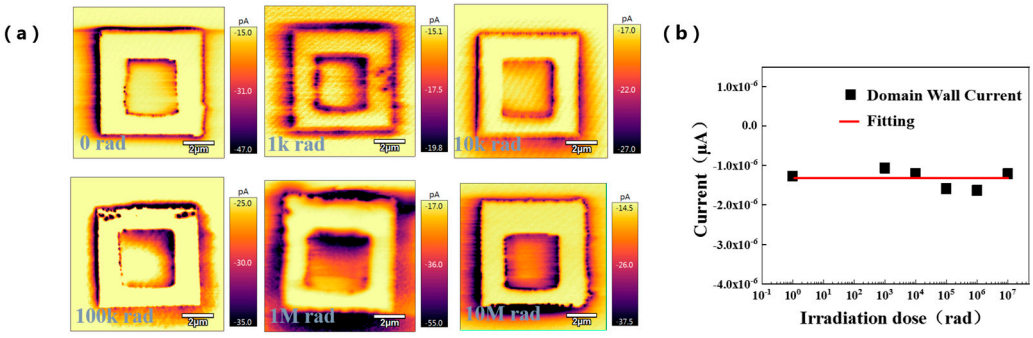

Figure 6. Domain wall current after 0 rad to 10 Mrad gamma irradiation: (**a**) c−AFM scan after various doses of irradiation at −7 V; (**b**) domain wall currents after different total doses of gamma irradiation.

In fact, gamma rays interact with matter in a variety of ways. For γ−rays with energies below 30 MeV, there are three predominant modalities: the photoelectric effect, the electron pair effect, and the Compton effect. Medium−energy γ−rays and absorbing substances with low atomic numbers mainly undergo the Compton effect. From the two photon

energies of the γ−rays, it is clear that the reaction between the γ−rays and the switched domains is mainly the Compton effect [34]. In the Compton effect, there are both elastic and inelastic collisions between photons and electrons. When a photon collides with an electron, the photon is scattered while the electron gains kinetic energy and recoils, but the total energy and total momentum remain conserved, it is an elastic collision. Inelastic collisions occur when a partial loss of energy occurs during the collision (e.g., part of the energy of the incident photon is used to overcome the binding energy of the electrons in the atom) [35].

Therefore this paper proposes a model for the switching of domains by gamma irradiation based on the Compton effect [36]. Li^+ was chosen as the object of study for three reasons: Firstly, Li^+ is more susceptible to shock and movement under high−energy radiation due to its small atomic number and much lighter mass than Nb^{5+} and O^{2-}. Secondly, Li^+ is located in a relatively unstable position in the lattice and is prone to migration when exposed to radiation. Finally, the bond energy between Li^+ and O^{2-} is relatively low, which makes it easier to be excited and moved when subjected to gamma ray impact [37].

During the irradiation process, gamma particles mainly collide with electrons. Since the cross−section of the collision between the gamma particle and the atom is very small, direct collision between gamma particles and atoms is considered negligible. In this work, 200 rad/s gamma particles were injected into the LN thin film. Outer−layer electrons of atoms turn into high−energy electrons by colliding with gamma particles. The high−energy electrons and collided gamma particles continue to transfer energy to other electrons and atoms. The energy of the photon is at its maximum when the direction of the incident photon is at the same angle as the electron exit angle at which the Compton effect occurs ($\theta = 0^\circ$). When the Compton electron exit angle is opposite to the direction of the incident photon ($\theta = \pi$), the photon energy is at a minimum, which is called backscattering. So, the photon energy is minimum at $\theta = \pi$ and the target particle gains maximum energy. The maximum energy (W_γ) transferred from the gamma photon to the target particle can be calculated using the following equation [38].

$$W_\gamma = \frac{2E_\gamma^2}{mc^2 + 2E_\gamma} \tag{1}$$

where E_γ is the energy carried by the gamma particles, m is the mass of the target particle being collided, and c is the speed of light. From the LN domain switching perspective, Li^+ and Nb^{5+} receive energy and move to another position, which is the opposite phase. Although initial gamma particles cannot collide with atoms directly, high−energy electrons and scattered gamma particles can still transfer energy to atoms. Li^+ of LN under gamma irradiation is shown in Figure 7a: gamma particles collide with peripheral electrons, unable to transfer energy to Li^+, directly; Figure 7b: high energy electrons created by gamma particles colliding and gamma particles that still possess energy after the collision transfer energy to Li^+; Figure 7c: Li^+ vibrates irregularly and consumes energy by heat dissipation (W_t); and Figure 7d: when the Li^+ energy accumulation reach domain switch energy (W_s), it moves through the oxygen plane which means domain switching is completed. In the possession of gamma irradiation, there are two powers: the power of atom−max irregularity thermal motion (P_t) and the power of gamma irradiation (P_γ). When $P_t \geq P_\gamma$, all irradiation energy is consumed by the atom's irregular thermal motion without energy accumulation. When $P_t < P_\gamma$, unconsumed energy accumulates in the atom, with a rate of $P_\gamma - P_t$. At this moment, the energy and power of the domain can be expressed by the following equation:

$$W_s = (P_\gamma - P_t)t \tag{2}$$

$$W_s = W_\gamma - W_T \tag{3}$$

where t is time. W_s is about the same order as the energy of 1 krad gamma irradiation. In this case, the switched domain structure was not damaged by the 10 Mrad gamma irradiation.

The reasons why the switched domain was not broken falls into three main categories: Firstly, $LiNbO_3$ belongs to the tripartite crystal system and its crystal structure shows high stability under radiation. Secondly, The oxygen ion displacement energy of $LiNbO_3$ is 53 eV, which corresponds to the incident electron energy threshold of about 0.33–0.35 MeV [39]. Therefore, $LiNbO_3$ is not prone to generate a large number of electron−hole pairs when irradiated, reducing irradiation−induced defects. Finally, In Figure 7c it is shown that Li^+ vibrates irregularly and consumes the vast majority of the energy delivered by the gamma rays through heat dissipation (W_t). Although the energy required for domain switching is comparable to that of a 1 krad gamma irradiation, most of the energy from a 1 krad gamma irradiation is consumed in the irregular thermal motion of the atoms. Therefore, the domain of LN has strong resistance to gamma irradiation.

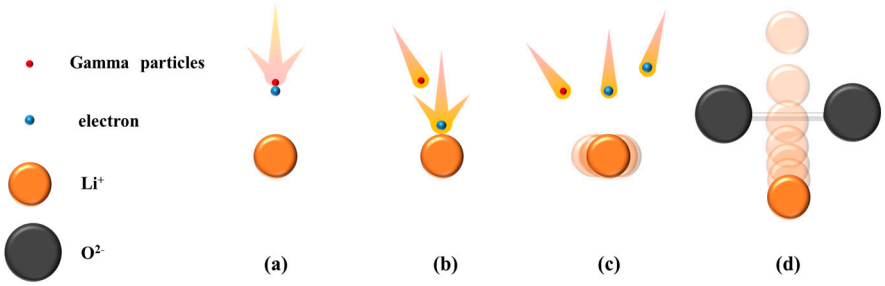

Figure 7. Diagram of gamma particles transferring energy to Li^+: (**a**) gamma particle collides with an electron, turns it into high energy electron; (**b**) energetic electron and scattered gamma particles collide with Li^+; (**c**) Li^+ consumes energy through random thermal motion; (**d**) after energy accumulation exceeds the threshold, Li^+ moves through oxygen plane.

X−ray diffraction (XRD), being a pivotal technique for physical phase analysis, serves as a reliable method to assess the impact of irradiation on the lattice of ferroelectric materials. When a beam of X−rays is incident on a crystal, the X−rays scattered by different atoms interfere with each other, resulting in enhanced X−ray diffraction in specific directions, and the direction and intensity of the diffraction lines provide feedback on the internal crystalline phase and crystal structure of the material. The fundamental basis for X−ray diffraction analysis is the Bragg equation:

$$2d\sin\theta = n\lambda \quad (4)$$

where d is the crystal plane spacing, n is the number of reflection levels, θ is the Bragg angle; and λ is the wavelength of X−rays. The crystallographic structure was analyzed using an Ultima IV type (Rigaku, Tokyo, Japan) X−ray diffractometer with a scanning range of 20°–80°, a scanning step of 0.02°, and a scanning rate of 10°/min. As shown in Figure 8, to highlight the (006) characteristic peak of the LN, the 2−theta was selected from 38.76° to 38.96°. The peak at 38.84° is from the LN substrate and the peak at 38.90° is from the LN film [40]. The very small deviation (~0.06°) between the LN substrate and the LN film comes from a slight difference in the cutting angle. As can be obtained from Figure 8, there is no displacement of the (006) characteristic peak when the total dose of gamma irradiation goes from 1 krad to 100 krad, indicating that the LN lattice is not damaged. At a total gamma irradiation dose of 1 Mrad, the characteristic peak of (006) shows a small displacement, but not more than 0.02°. The peaks and peak widths become progressively smaller as the total gamma irradiation dose goes from 1 krad to 1 Mrad, but do not show much change. Therefore, the total dose of γ−ray below 1Mrad cannot cause damage to the lattice of LN and denature it.

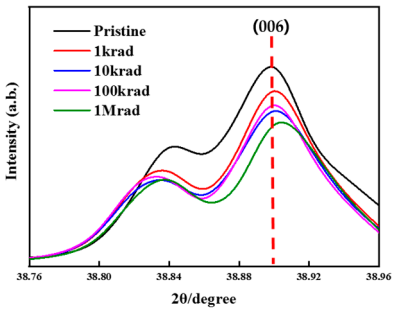

Figure 8. XRD spectra of the γ−ray irradiated LN thin films, doses up to 1 Mrad.

4. Conclusions

In summary, the irradiation resistance of LN domain structures was studied in this work. Initially, we outlined the preparation process for the 700 nm Z−cut LN bonding sheet. The essence of the $LiNbO_3$ structural domain switching is illustrated from the crystal structure point of view as the movement of Li^+ and Nb^{5+}, and the precise preparation of five same−domain structures was realized by PFM. Subsequently, five samples were irradiated from 1 krad to 10 Mrad. Domain wall current was measured at various sample voltages using the ORCA mode of c−AFM, with a sample voltage of −7 V being determined as optimal. All samples' domain structure and DWC remained stable after irradiation. We explain the irradiation resistance of the LN domain from an atomic perspective, which describes the relationship between irradiation power and domain switching power. This research lends support to the utilization of ferroelectric domain engineering devices in irradiation environments.

Author Contributions: Conceptualization, J.L., J.H. and W.G.; methodology, J.L., J.H. and M.X.; validation, J.L., L.N. and W.G.; formal analysis, J.L. and J.H.; investigation, B.Z., X.Q. and H.L.; resources, L.N.; data curation, J.L. and J.H.; writing—original draft preparation, J.L. and J.H.; writing—review and editing, J.L., X.C. and W.G. All authors have read and agreed to the published version of the manuscript.

Funding: This work was supported by the National Natural Science Foundation of China (62171415), the Fundamental Research Program of Shanxi Province (202203021223005, 202203021222068), the Fund Program for the Scientific Activities of Selected Returned Overseas Professionals in Shanxi Province (20230015), the Central Guidance on Local Science and Technology Development Fund of Shanxi Province (YDZJSX20231A028), the National Defense Fundamental Research Project and the Guangdong Basic and Applied Basic Research Foundation (2023A1515110108).

Data Availability Statement: The data that support the findings of this study are available from the corresponding author, due to privacy.

Conflicts of Interest: Authors Jinlong He, and Liya Niu were employed by the company Faraday Technology Corporation SZ and Jiangsu Institute of Advanced Semiconductors Ltd. The remaining authors declare that the research was conducted in the absence of any commercial or financial relationships that could be construed as a potential conflict of interest.

References

1. Spahn, M. X-ray detectors in medical imaging. *Nucl. Instrum. Methods Phys. Res. Sect. A Accel. Spectrometers Detect. Assoc. Equip.* **2013**, *731*, 57–63. [CrossRef]
2. Rehani, M.M. Patient radiation exposure and dose tracking: A perspective. *J. Med. Imaging* **2017**, *4*, 031206. [CrossRef]
3. Komotar, R.J.; Otten, M.L.; Moise, G.; Connolly, E.S., Jr. Radiotherapy plus concomitant and adjuvant temozolomide for glioblastoma-a critical review. *Clin. Med. Oncol.* **2008**, *2*, 421–422. [CrossRef]
4. Suehle, J.S.; Vogel, E.M.; Roitman, P.; Conley, J.F.; Johnston, A.H.; Wang, B.; Bernstein, J.B.; Weintraub, C.E. Observation of latent reliability degradation in ultrathin oxides after heavy-ion irradiation. *Appl. Phys. Lett.* **2002**, *80*, 1282–1284. [CrossRef]
5. Palumbo, F.; Debray, M.; Vega, N.; Quinteros, C.; Kalstein, A.; Guarin, F. Evolution of the gate current in 32 nm MOSFETs under irradiation. *Solid-State Electron.* **2016**, *119*, 19–24. [CrossRef]
6. Conley, J.F.; Suehle, J.S.; Johnston, A.H.; Wang, B.; Miyahara, T.; Vogel, E.M.; Bernstein, J.B. Heavy-ion-induced soft breakdown of thin gate oxides. *IEEE Trans. Nucl. Sci.* **2001**, *48*, 1913–1916. [CrossRef]

7. Kumar, K.V.A.; Raghavendra, M.; Hegde, V.N.; Prakash, A.P.G.; Ravikumar, H.B. Gamma irradiation induced microstructural modification and electrical conductivity of bakelite resistive plate chamber material. *J. Radioanal. Nucl. Chem.* **2021**, *327*, 821–829. [CrossRef]
8. Li, Z.; Zeng, J.; Sun, Y.; Liu, J.; Zhai, P.; Liu, T.; Bi, J.; Zhang, Z.; Zhang, S.; Hu, P.; et al. Latent Reliability Degradation of Ultrathin Amorphous HfO2 Dielectric After Heavy Ion Irradiation: The Impact of Nano-Crystallization. *IEEE Electron. Device Lett.* **2019**, *40*, 1634–1637. [CrossRef]
9. Mekki, J.; Moll, M.; Glaser, M.; Guatelli, S.; Pia, M.G.; Ravotti, F.; Dusseau, L. Packaging effects on radFET sensors for High Energy Physics Experiments. In Proceedings of the 2008 European Conference on Radiation and Its Effects on Components and Systems, Jyvaskyla, Finland, 10–12 September 2008; pp. 225–230.
10. Baldini, L.; Brez, A.; Himel, T.; Johnson, R.P.; Latronico, L.; Minuti, M.; Nelson, D.; Sadrozinski, H.F.W.; Sgro, C.; Spandre, G.; et al. Fabrication of the GLAST Silicon Tracker Readout Electronics. *IEEE Trans. Nucl. Sci.* **2006**, *53*, 3013–3020. [CrossRef]
11. Brucker, G.J.; Kronenberg, S.; Gentner, F. Effects of package geometry, materials, and die design on energy dependence of pMOS dosimeters. *IEEE Trans. Nucl. Sci.* **1995**, *42*, 33–40. [CrossRef]
12. Zanata, M.; Wrachien, N.; Cester, A. Ionizing Radiation Effect on Ferroelectric Nonvolatile Memories and Its Dependence on the Irradiation Temperature. *IEEE Trans. Nucl. Sci.* **2008**, *55*, 3237–3245. [CrossRef]
13. Coic, Y.M.; Musseau, O.; Leray, J.L. A study of radiation vulnerability of ferroelectric material and devices. *IEEE Trans. Nucl. Sci.* **1994**, *41*, 495–502. [CrossRef]
14. Scott, J.F.; Araujo, C.A.; Meadows, H.B.; McMillan, L.D.; Shawabkeh, A. Radiation effects on ferroelectric thin-film memories: Retention failure mechanisms. *J. Appl. Phys.* **1989**, *66*, 1444–1453. [CrossRef]
15. Tong, L.; Peng, Z.R.; Lin, R.F.; Li, Z.; Wang, Y.L.; Huang, X.Y.; Xue, K.H.; Xu, H.Y.; Liu, F.; Xia, H.; et al. 2D materials-based homogeneous transistor-memory architecture for neuromorphic hardware. *Science* **2021**, *373*, 1353–1358. [CrossRef]
16. Chai, X.; Jiang, J.; Zhang, Q.; Hou, X.; Meng, F.; Wang, J.; Gu, L.; Zhang, D.W.; Jiang, A.Q. Nonvolatile ferroelectric field-effect transistors. *Nat. Commun.* **2020**, *11*, 2811. [CrossRef]
17. Bazzan, M.; Sada, C. Optical waveguides in lithium niobate: Recent developments and applications. *Appl. Phys. Rev.* **2015**, *2*, 040603. [CrossRef]
18. Poberaj, G.; Hu, H.; Sohler, W.; Günter, P. Lithium niobate on insulator (LNOI) for micro-photonic devices. *Laser Photonics Rev.* **2012**, *6*, 488–503. [CrossRef]
19. Sun, X.; Su, Y.J.; Gao, K.W.; Guo, L.Q.; Qiao, L.J.; Chu, W.Y. The effect of humidity on nano-scaled domain switching in $LiNbO_3$ single crystal. *J. Appl. Phys.* **2011**, *110*, 014103. [CrossRef]
20. Kirbus, B.; Godau, C.; Wehmeier, L.; Beccard, H.; Beyreuther, E.; Haußmann, A.; Eng, L.M. Real-Time 3D Imaging of Nanoscale Ferroelectric Domain Wall Dynamics in Lithium Niobate Single Crystals under Electric Stimuli: Implications for Domain-Wall-Based Nanoelectronic Devices. *ACS Appl. Nano Mater.* **2019**, *2*, 5787–5794. [CrossRef]
21. Lu, H.; Tan, Y.; McConville, J.P.V.; Ahmadi, Z.; Wang, B.; Conroy, M.; Moore, K.; Bangert, U.; Shield, J.E.; Chen, L.Q.; et al. Electrical Tunability of Domain Wall Conductivity in LiNbO(3) Thin Films. *Adv. Mater.* **2019**, *31*, e1902890. [CrossRef]
22. Seidel, J.; Martin, L.W.; He, Q.; Zhan, Q.; Chu, Y.H.; Rother, A.; Hawkridge, M.E.; Maksymovych, P.; Yu, P.; Gajek, M.; et al. Conduction at domain walls in oxide multiferroics. *Nat. Mater.* **2009**, *8*, 229–234. [CrossRef]
23. Niu, L.; Qiao, X.; Lu, H.; Fu, W.; Liu, Y.; Bi, K.; Mei, L.; You, Y.; Chou, X.; Geng, W. Diode-Like Behavior Based on Conductive Domain Wall in LiNbO Ferroelectric Single-Crystal Thin Film. *IEEE Electron. Device Lett.* **2023**, *44*, 52–55. [CrossRef]
24. Geng, W.; He, J.; Qiao, X.; Niu, L.; Zhao, C.; Xue, G.; Bi, K.; Mei, L.; Wang, X.; Chou, X. Conductive Domain-Wall Temperature Sensors of LiNbO3 Ferroelectric Single-Crystal Thin Films. *IEEE Electron. Device Lett.* **2021**, *42*, 1841–1844. [CrossRef]
25. Wang, C.; Zhang, M.; Chen, X.; Bertrand, M.; Shams-Ansari, A.; Chandrasekhar, S.; Winzer, P.; Loncar, M. Integrated lithium niobate electro-optic modulators operating at CMOS-compatible voltages. *Nature* **2018**, *562*, 101–104. [CrossRef]
26. Ellenbogen, T.; Voloch-Bloch, N.; Ganany-Padowicz, A.; Arie, A. Nonlinear generation and manipulation of Airy beams. *Nat. Photonics* **2009**, *3*, 395–398. [CrossRef]
27. Boes, A.; Corcoran, B.; Chang, L.; Bowers, J.; Mitchell, A. Status and Potential of Lithium Niobate on Insulator (LNOI) for Photonic Integrated Circuits. *Laser Photonics Rev.* **2018**, *12*, 1700256. [CrossRef]
28. Lian, J.; Chai, X.; Wang, C.; Hu, X.; Jiang, J.; Jiang, A. Sub 20 nm-Node $LiNbO_3$ Domain—Wall Memory. *Adv. Mater. Technol.* **2021**, *6*, 20012196. [CrossRef]
29. *MIL-STD-883f*; Department of Defense Test Method Standard: Microcircuits. United States Department of Defense: Washington, DC, USA, 2010.
30. Ren, Y.; Zhu, M.; Xu, D.; Liu, M.; Dai, X.; Wang, S.; Li, L.; Juoi, J.M. Overview on Radiation Damage Effects and Protection Techniques in Microelectronic Devices. *Sci. Technol. Nucl. Install.* **2024**, *2024*, 1–17. [CrossRef]
31. Park, Y.B.; Min, B.; Vahala, K.J.; Atwater, H.A. Integration of Single-Crystal $LiNbO_3$ Thin Film on Silicon by Laser Irradiation and Ion Implantation– Induced Layer Transfer. *Adv. Mater.* **2006**, *18*, 1533–1536. [CrossRef]
32. Mann, A.K. Elastic Scattering of Gamma Rays. *Phys. Rev.* **1956**, *101*, 4–8. [CrossRef]
33. Inbar, I.; Cohen, R.E. Comparison of the electronic structures and energetics of ferroelectric $LiNbO_3$ and $LiTaO_3$. *Phys. Rev. B Condens. Matter* **1996**, *53*, 1193–1204. [CrossRef]
34. Povh, B.; Rith, K.; Scholz, C.; Zetsche, F. *Particles and Nuclei: An Introduction to the Physical Concepts*; Particles and Nuclei: An Introduction to the Physical Concepts; Springer: Berlin/Heidelberg, Germany, 2006.

35. McGhee, K.E. A century of Compton scattering. *Nat. Rev. Phys.* **2023**, *5*, 322. [CrossRef]
36. Pollyceno, L.S.; Ribeiro, A.D. Wave-particle duality using the Compton effect. *arXiv* **2020**, arXiv:2005.02939. [CrossRef]
37. Veithen, M.G.P. First-principles study of the dielectric and dynamical properties of lithium niobate—Art. no. 214302. *Phys. Rev. B. Condens. Matter* **2002**, *65*, 214302. [CrossRef]
38. Lee, W.; Jo, A.; Lee, T.; Chu, D.; Chung, Y.H. Monte Carlo Simulation on 4p Field of View Compact Compton Camera Using Scintillators. *J. Korean Phys. Soc.* **2010**, *56*, 20–27. [CrossRef]
39. Popov, A.I.; Kotomin, E.A.; Maier, J. Basic properties of the F-type centers in halides, oxides and perovskites. *Nucl. Instrum. Methods Phys. Res. Sect. B Beam Interact. Mater. At.* **2010**, *268*, 3084–3089. [CrossRef]
40. Han, H.; Cai, L.; Hu, H. Optical and structural properties of single-crystal lithium niobate thin film. *Opt. Mater.* **2015**, *42*, 47–51. [CrossRef]